

Experimental observation of topological Fermi arcs in type-II Weyl semimetal MoTe₂

Ke Deng,^{1,*} Guoliang Wan,^{1,*} Peng Deng,^{1,*} Kenan Zhang,¹ Shijie Ding,¹ Eryin Wang,¹ Mingzhe Yan,¹ Huaqing Huang,¹ Hongyun Zhang,¹ Zhilin Xu,¹ Jonathan Denlinger,² Alexei Fedorov,² Haitao Yang,^{1,3} Wenhui Duan,^{1,4} Hong Yao,^{5,4} Yang Wu,^{3,†} Shoushan Fan,^{1,3,4} Haijun Zhang,^{6,7} Xi Chen,^{1,4,†} and Shuyun Zhou^{1,4,†}

¹*State Key Laboratory of Low Dimensional Quantum Physics and Department of Physics, Tsinghua University, Beijing 100084, China*

²*Advanced Light Source, Lawrence Berkeley National Laboratory, Berkeley, California 94720, USA*

³*Tsinghua-Foxconn Nanotechnology Research Center, Tsinghua University, Beijing 100084, China*

⁴*Collaborative Innovation Center of Quantum Matter, Beijing, China*

⁵*Institute for Advanced Study, Tsinghua University, Beijing 100084, China*

⁶*National Laboratory of Solid State Microstructures and School of Physics, Nanjing University, Nanjing 210093, China*

⁷*Collaborative Innovation Center of Advanced Microstructures, Nanjing, China*

(Dated: March 8, 2022)

*These authors contribute equally to this work.

†Correspondence should be sent to wuyangthu@mail.tsinghua.edu.cn, xc@mail.tsinghua.edu.cn and syzhou@mail.tsinghua.edu.cn

Weyl semimetal is a new quantum state of matter [1–12] hosting the condensed matter physics counterpart of relativistic Weyl fermion [13] originally introduced in high energy physics. The Weyl semimetal realized in the TaAs class features multiple Fermi arcs arising from topological surface states [10, 11, 14–16] and exhibits novel quantum phenomena, e.g., chiral anomaly induced negative magnetoresistance [17–19] and possibly emergent supersymmetry [20]. Recently it was proposed theoretically that a new type (type-II) of Weyl fermion [21], which does not have counterpart in high energy physics due to the breaking of Lorentz invariance, can emerge as topologically-protected touching between electron and hole pockets. Here, we report direct spectroscopic evidence of topological Fermi arcs in the predicted type-II Weyl semimetal MoTe_2 [22–24]. The topological surface states are confirmed by directly observing the surface states using bulk- and surface-sensitive angle-resolved photoemission spectroscopy (ARPES), and the quasi-particle interference (QPI) pattern between the two putative Fermi arcs in scanning tunneling microscopy (STM). Our work establishes MoTe_2 as the first experimental realization of type-II Weyl semimetal, and opens up new opportunities for probing novel phenomena such as exotic magneto-transport [21] in type-II Weyl semimetals.

In the Brillouin zone of a type-I Weyl semimetal, the linear dispersing and non-degenerate bands cross each other at the Weyl points (Fig. 1(a)). These band-topology protected Weyl points can only be created or annihilated in pairs according to the no-go theorem [1]. When projected onto the surface, the Weyl points are connected by the topologically protected Fermi arcs (Fig. 1(b)) [2]. In contrast to the type-I Weyl fermions in TaAs class or compressively-strained HgTe [12] which have point-like Fermi surface, the type-II Weyl fermions emerge at the boundary between electron and hole pockets when the cones are tilted significantly (Fig. 1(c)), and there are finite density of states at the Fermi energy E_F (Fig. 1(d)) [21]. The difference in the Fermi surfaces of these two types of Weyl semimetals is expected to lead to distinctive response to magnetic fields [21].

Type-II Weyl fermion has been predicted in the orthorhombic T_d phase of WTe_2 [21], which breaks the inversion symmetry and shows unusual transport properties [25]. However, the small momentum separation of the Weyl points (0.7% of the Brillouin zone) and the extremely small size of the arcs [21] make it exceptionally challenging to resolve the Fermi

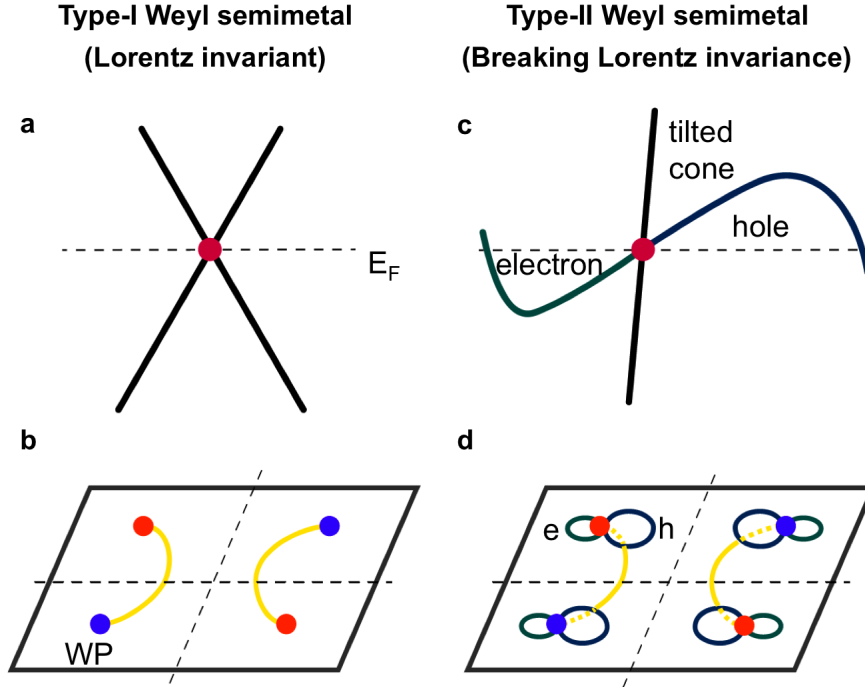


FIG. 1: **Schematic drawings for a comparison between type-I and type-II Weyl semimetals.** (a, c) Schematic dispersions for type-I (a) and type-II (c) Weyl fermion near E_F . The Weyl points are labeled by red dots. (b, d) Fermi surfaces for type-I (b) and type-II (d) Weyl semimetals in the simplest case with a minimum number of four Weyl points. The bulk Weyl points are labeled by red and blue dots, and the Fermi arcs from the topological surface states are labeled as yellow curves. For type-II Weyl semimetals, part of the Fermi arcs (yellow dotted curves) may be shadowed by the bulk electron and hole pockets.

arcs in WTe_2 by ARPES. A promising solution is provided by the prediction that the Fermi arcs can be significantly enlarged in MoTe_2 [22, 23] or $\text{Mo}_x\text{W}_{1-x}\text{Te}_2$ [26]. Among these candidate materials, MoTe_2 is particularly interesting because of the reported superconductivity [27] and the predicted topological phase transition induced by temperature or strain [22]. Although the electronic structures of WTe_2 [28–30] and $\text{Mo}_x\text{W}_{1-x}\text{Te}_2$ [31] have been experimentally studied, so far there is no conclusive evidence on the existence of Fermi arcs. Here by combining two surface sensitive probes - ARPES and STM, we provide direct experimental evidence of the Fermi arcs at the boundary between electron and hole pockets in MoTe_2 . The experimental dispersions extracted from ARPES, STM are in good agreement

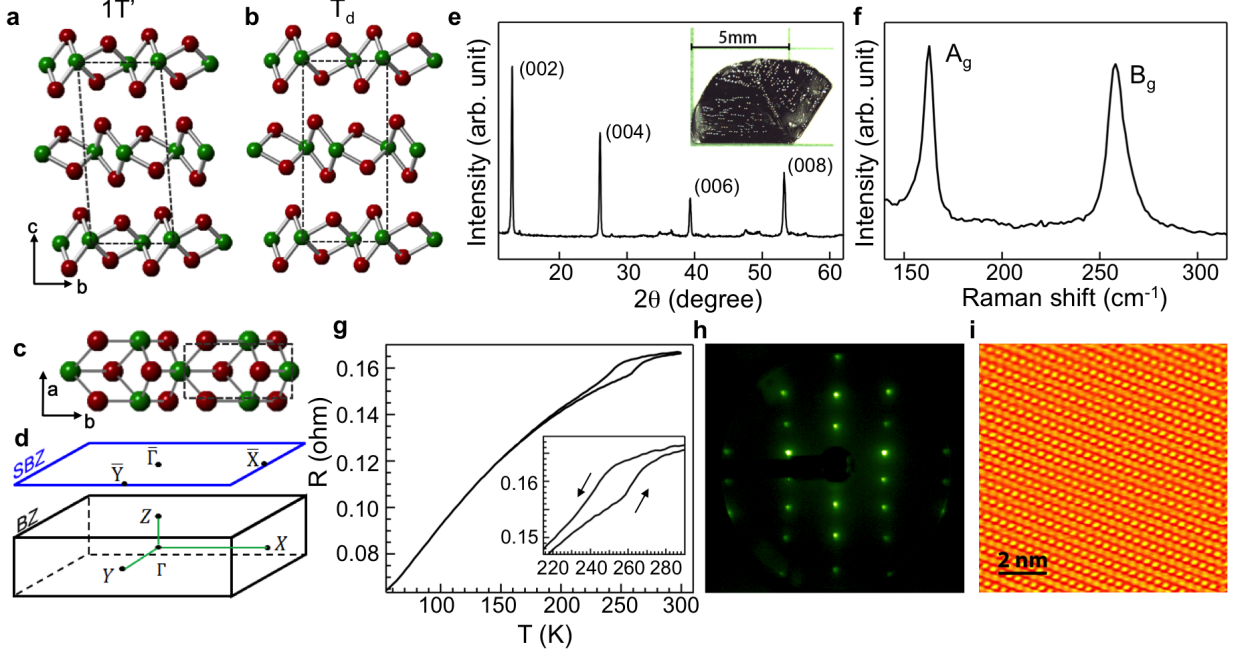


FIG. 2: **Crystal structure of MoTe₂.** (a-b) Crystal structures of MoTe₂ in the 1T' (a) and T_d (b) phases. Green balls are Mo atoms and red balls are Te atoms. (c) The in-plane crystal structure. (d) Bulk and projected surface Brillouin zone. (e) XRD of MoTe₂ measured at room temperature (1T' phase). The inset shows a picture of the few mm size single crystal. (f) Raman spectrum measured at room temperature. (g) Transport measurement shows a first order phase transition between the 1T' phase and the T_d phase. (h) LEED pattern taken in the T_d phase at beam energy of 180 eV. (i) The STM topography (bias -50 mV, tunneling current 0.05 nA) taken at 4.2 K shows a rectangular lattice with the lattice constants of $a = 3.5 \text{ \AA}$, $b = 6.3 \text{ \AA}$. The cleaved surface is terminated by Te atoms. The center and corner atoms of a rectangular unit are different in height and exhibit distinct contrast. The dI/dV spectrum is shown in the supplementary information.

with the calculated dispersions for the topological surface states, establishing MoTe₂ as a type-II Weyl semimetal.

MoTe₂ is polymorphic with three different structures: hexagonal (α -phase, or 2H phase), monoclinic (β -phase, or 1T' phase) and orthorhombic (γ -phase, or T_d phase). The 1T' phase has a distorted CdI₂ structure (Fig. 2(a)) that crystalizes in the centrosymmetric space group P2₁/m. The Mo atoms are coordinated by eight Te atoms but shifted from the center of the Te octahedra, resulting in the zigzag chains along the b axis. The bonding between the

shifted Mo atoms corrugates the Te sheets and distorts the Te octahedra [32, 33], causing the c axis to incline at an angle of $\sim 93.9^\circ$ [32]. A temperature induced phase transition from T_d to the $1T'$ phase has been reported between 240 K to 260 K [32]. The low-temperature T_d phase (Fig. 2(b)) shares the same in-plane crystal structure (Fig. 2(c)) as $1T'$ but has a vertical (90°) stacking and belongs to the non-centrosymmetric space group $Pmn2_1$. Weyl fermions are only possible in the T_d phase where the inversion symmetry is broken. The Brillouin zone of T_d phase is shown in Fig. 2(d).

Figure 2(e) shows the X-ray diffraction (XRD) intensity of the high quality MoTe_2 single crystal at room temperature ($1T'$ phase). The Raman spectrum in Fig. 2(f) shows A_g and B_g vibrational modes at ~ 160 and 260 cm^{-1} respectively, consistent with other report [34]. The resistance measurement (Fig. 2(g)) confirms the first order phase transition between the T_d and $1T'$ phases at ~ 260 K, in agreement with previous results [32]. The high crystallinity of the samples is revealed by the sharp diffraction peaks (Fig. 2(h)) in the low energy electron diffraction (LEED) pattern measured on a freshly cleaved sample in the T_d phase. The atomically resolved STM topography in Fig. 2(i) further confirms the high quality of the MoTe_2 crystal.

Figure 3(a-c) shows a comparison of the electronic structure of MoTe_2 in the T_d phase measured by ARPES with band structure calculation along the a -axis ($\bar{X}-\bar{\Gamma}-\bar{X}$) direction. The ARPES spectral intensity is determined by the dipole matrix elements and thereby depends both on the electron wave function and light polarization. To resolve the dispersions of multiple pockets, we use UV light with both horizontal (p) and vertical (s) polarizations. The electron pockets away from the Γ point are better resolved with the p-polarization light (Fig. 3(b)), while the s-polarization light clearly resolves the pockets around the Γ point (Fig. 3(c)). The bands that disperse significantly with k_z overlap to form continuously filled contours, while those with strong surface state characteristics show up as sharp features in the intensity maps. The measured dispersions are in good agreement with the first-principles calculations.

We search for possible signatures of the Fermi arcs in the ARPES intensity maps by comparing ARPES data taken with bulk sensitive laser source at 6.3 eV (penetration depth of $\approx 30 \text{ \AA}$) and surface sensitive UV source at 20-90 eV (penetration depth of a few \AA). Figure 3(d) shows the calculated projected Fermi surface map. There are two electron pockets with bell-like shape on both sides of the Γ point. The hole pocket with bowtie shape centered

around the Γ point crosses the electron pockets at eight Weyl points (W1 and W2) [22, 23]. Fermi arcs are expected to emerge between those Weyl points with opposite chiralities [21–23]. The small momentum separation between these pockets with the surface states near the Weyl points makes it challenging to distinguish them, and comparison of bulk sensitive with surface sensitive ARPES data is critical to separate their contributions. Figure 3(e,f) shows the measured Fermi surface maps with bulk sensitive laser source with light polarizations perpendicular to the b and a axis respectively. The electron pockets are clearly observed with an overall uniform intensity around the pocket in Figure 3(e) (blue broken curve), while the bowtie-shaped hole pocket is more clearly observed in Figure 3(f) (black curve). These observations are in agreement with the bulk band structure. Figure 3(g) shows the Fermi surface map using 32.5 eV photon energy. The most striking feature in the intensity map is the two sharp arcs (pointed by red arrow) with much stronger intensity than the electron pockets. The arcs are observed at the edge of the continuously filled electron pockets, and they terminate at the momentum positions close to the calculated Weyl points W2. This suggests that the observed arcs are likely topologically protected surface states. Figure 3(h-k) shows the zoom-in intensity maps with ultra-high resolution at energies from E_F to -60 meV. With increasing binding energy, the bell-shaped electron pockets (indicated by blue arrows) decrease in size and a significant separation between the electron pocket and the hole pocket is clearly observed at -40 meV. Moreover, the two sharp arc-like features are identified in the intensity maps at -60 meV. The combination of bulk and surface sensitive ARPES intensity maps point to Fermi arcs at the boundary between electron and hole pockets as schematically shown in Figure 3(l).

To further confirm the topological surface states, we compare the measured dispersion along the \bar{X} - $\bar{\Gamma}$ - \bar{X} direction with theoretical calculation in Figure 4. Different photon energies and light polarizations are used to distinguish electronic states from different pockets and to further distinguish the bulk states from surface states. Circular polarized UV light can enhance the contribution from the small electron pocket away from the Γ point (pointed to by arrow in panel (d)). Data taken with laser source or higher energy UV source show an enhancement of the bulk states, and it is clear that the dispersion around the Γ point changes significantly with photon energies. Most importantly, a shoulder-like dispersion similar to the zoom-in dispersion of the topological surface states in Figure 4(b) is observed at the boundary between electron and hole pockets in all data. Moreover, this band does not dis-

perse with different photon energies, confirming that it is dominated by surface states. The comparison with band structure calculation shows an overall agreement, providing strong evidence that this shoulder-like dispersion is indeed from the topological surface states.

The observed Fermi arcs reside on the two-dimensional (2D) crystal surface. The surface nature of the Fermi arcs is further confirmed by the QPI pattern using STM. Universal signatures of Fermi arcs in QPI on the surface of Weyl semimetals have been established by Ref. 24. Various defects on the surface elastically scatter the electrons and induce the QPI pattern. In the surface Brillouin zone, the extremal pairs of \vec{k}_i and \vec{k}_f on a 2D constant energy contour, where \vec{k}_i and \vec{k}_f are the initial and final wave vectors, contribute dominantly to the spatial interference pattern of the local electron density of states (LDOS) [35]. The spatial variation of LDOS at a certain energy is the sum of the contributions from all the extremal pairs on the constant energy contour and measured by the differential conductance (dI/dV) mapping with spatial resolution. The features in the Fourier transform of dI/dV mapping correspond to the scattering vector $\vec{Q} = \vec{k}_f - \vec{k}_i$ of the extremal pairs. QPI is more sensitive to the surface states or states with small k_z dependence than to the bulk ones with strong k_z dependence since the latter cannot host the “extreme pairs”. In this sense, QPI is advantageous in studying type-II Weyl semimetal MoTe₂, where the Fermi arcs and the projected bulk pockets are overlapped in energy.

For a pair of Fermi arcs, three scattering wave vectors (Fig. 5(a)), labeled q_1 , q_2 , and q_3 , might be expected to appear in QPI. Among them, q_3 is forbidden due to the requirement of the time-reversal symmetry in the system. Similar forbidden scattering was also experimentally observed in the surface states of topological insulators with time-reversal symmetry [36]. The intra-arc scattering q_2 is difficult to resolve because it overlaps with the large intensity stemming from other features in the electronic structure. Only the inter-arc scattering q_1 can generate visible features along the Γ -X direction in QPI. Figures 5(b-l) display the fast Fourier transform (FFT) of the dI/dV maps at various energies. Between -10 mV and -90 mV, the scattering wave vector q_1 is clearly resolved and indicated by black arrows. The dispersions extracted from the energy dependent scattering wave vector is plotted in panel (m). Comparison with ARPES data and band structure calculation shows that this scattering vector is related to the topological Fermi arcs.

In summary, by combining two surface sensitive experimental probes - STM, ARPES - with theoretical calculations, we provide direct and strong experimental evidence for the

existence of the topological surface states, establishing it as a type-II Wey semimetal. The experimental study opens up new opportunities for investigating exotic topological quantum states that cannot be realized in high energy physics.

Note added. During revision of this manuscript for resubmission, we became aware of related work by L. Huang *et al.* [37].

Methods

Sample growth. High quality β -MoTe₂ single crystals were grown by chemical vapor transport using polycrystalline MoTe₂ as precursors. Polycrystalline MoTe₂ was synthesized by directly heating the stoichiometric mixture of high-purity Mo foil (99.95%, Alfa Aesar) and Te ingot (99.99%, Alfa Aesar) at 1073 K in a vacuum-sealed silica ampoule for 3 days. The as-grown MoTe₂ was then recrystallized by the chemical vapor transport method using powder TeCl₄ (99%, Aladdin) as transporting agent with a concentration of ≤ 2.7 mg/mL. Material transport occurred in a sealed silica ampoule in a tube furnace for 3 days. After the reaction, the ampoule was immediately quenched in cold water to obtain large size β -MoTe₂ single crystals.

ARPES measurement. ARPES measurements have been performed at BL4.0.1 of the Advanced Light Source using photon energies from 30.5 eV to 90 eV. The overall experimental energy resolution at 32.5 eV is better than 18 meV. The samples were cleaved and measured at 10 K in the T_d phase.

STM measurement. STM experiments were conducted on a Unisoku ultrahigh vacuum low temperature (down to 4.2 K) system equipped with *in situ* cleaving stage. The MoTe₂ single crystals were cleaved in ultrahigh vacuum (5×10^{-11} Torr) at room temperature and then transferred to STM to perform measurement at 4.2 K with a PtIr tip. QPI maps and dI/dV spectra were acquired using a lock-in amplifier at frequency of 913 Hz.

First-principles calculations.

The *ab-initio* calculations are carried out in the framework of the Perdew-Burke-Ernzerhof-type generalized gradient approximation of the density functional theory through employing the Vienna Ab initio simulation package (VASP) [38] with the projected augmented wave (PAW) method. The kinetic energy cutoff is fixed to 400 eV, and the \mathbf{k} -point mesh is taken as $12 \times 10 \times 6$ for the bulk calculations. The spin-orbit coupling effect is self-consistently included. The lattice constants and positions of atoms are all taken from experiments [22]. Maximally localized Wannier functions are employed to obtain the *ab-*

initio tight-binding model of semi-infinite systems with the (001) surface as the boundary to exhibit surface states and Fermi arcs. An iterative method is used to obtain the surface Green's function of the semi-infinite system.

- [1] Nielsen, H. B. & Ninomiya, M. The Adler-Bell-Jackiw anomaly and Weyl fermions in a crystal. *Physics Letters B* **130**, 389 (1983).
- [2] Wan, X., Turner, A.M., Vishwanath, A. & Savrasov, S.Y. Topological semimetal and Fermi-arc surface states in the electronic structure of pyrochlore iridates. *Phys. Rev. B* **83**, 205101 (2011).
- [3] Burkov, A.A. & Balents, L. Weyl Semimetal in a Topological Insulator Multilayer. *Phys. Rev. Lett.* **107**, 127205 (2011).
- [4] Xu, G., Weng, H., Wang, Z., Dai, X. & Fang, Z. Chern Semimetal and the Quantized Anomalous Hall Effect in HgCr_2Se_4 . *Phys. Rev. Lett.* **107**, 186806 (2011).
- [5] Yang, K.Y., Lu, Y.M. & Ran, Y. Quantum Hall effects in a Weyl semimetal: Possible application in pyrochlore iridates *Phys. Rev. B* **84**, 075129 (2011).
- [6] Hosur, P. & Qi, X. Recent developments in transport phenomena in Weyl semimetals. *C. R. Physique* **14**, 857 (2013).
- [7] Zhang, H., Wang, J., Xu, G., Xu, Y. & Zhang, S. C. Topological States in Ferromagnetic CdO/EuO Superlattices and Quantum Wells. *Phys. Rev. Lett.* **112**, 096804 (2014).
- [8] Liu, J. & Vanderbilt, D. Weyl semimetals from noncentrosymmetric topological insulators. *Phys. Rev. B* **90**, 155316 (2014).
- [9] Hirayama, M., Okugawa, R., Ishibashi, S., Murakami, S. & Miyake, T. Weyl Node and Spin Texture in Trigonal Tellurium and Selenium. *Phys. Rev. Lett.* **114**, 206401 (2015).
- [10] Weng, H., Fang, C., Fang, Z., Bernevig, B. A. & Dai, X. Weyl semimetal phase in noncentrosymmetric transition-metal monophosphides. *Phys. Rev. X* **5**, 011029 (2015).
- [11] Huang, S.-M. *et al.* A Weyl Fermion semimetal with surface Fermi arcs in the transition metal monopnictide TaAs class. *Nature Commun.* **6**, 7373 (2015).
- [12] Ruan, J. *et al.* Symmetry-protected ideal Weyl semimetal in HgTe-class materials. Preprint at <http://arxiv.org/abs/1511.08284> (2015).
- [13] Weyl, H. Elektron und gravitation. *I.Z. Phys.* **56**, 330-352 (1929).

- [14] Lv, B.Q. *et al.* Experimental discovery of Weyl semimetal TaAs. *Phys. Rev. X* **5**, 031013 (2015).
- [15] Xu, S.-Y. *et al.* Discovery of a Weyl fermion semimetal and topological Fermi arcs. *Science* **349**, 613 (2015).
- [16] Yang, L.X. *et al.* Weyl semimetal phase in the non-centrosymmetric compound TaAs. *Nature Phys.* **11**, 728 (2015).
- [17] Son, D. T. & Spivak, B. Z. Chiral anomaly and classical negative magnetoresistance of Weyl metals. *Phys. Rev. B* **88**, 104412 (2013).
- [18] Huang, X. *et al.* Observation of the chiral-anomaly-induced negative magnetoresistance in 3D Weyl semimetal TaAs. *Phys. Rev. X* **5**, 031023 (2015).
- [19] Zhang, C. *et al.* Observation of the Adler-Bell-Jackiw chiral anomaly in a Weyl semimetal. Preprint at <http://arxiv.org/abs/1503.02630> (2015).
- [20] Jian, S. K., Jiang, Y. F. & Yao, H. Emergent spacetime supersymmetry in 3D weyl semimetals and 2D dirac semimetals. *Phys. Rev. Lett.* **114**, 237001 (2015).
- [21] Soluyanov, A.A. *et al.* Type-II Weyl semimetals. *Nature* **527**, 495 (2015).
- [22] Sun, Y., Wu, S.C., Ali, M.N., Felser, C., & Yan, B. Prediction of Weyl semimetal in orthorhombic MoTe₂. *Phys. Rev. B* **92**, 161107 (2015).
- [23] Wang, Z. *et al.* MoTe₂: Weyl and line node topological metal. Preprint at <http://arxiv.org/abs/1511.07440> (2015).
- [24] Kourtis, S., Li, J., Wang, Z., Yazdani, A. & Bernevig, B. A. Universal signatures of Fermi arcs in quasiparticle interference on the surface of Weyl semimetals. Preprint at <http://arxiv.org/abs/1512.02646> (2015).
- [25] Ali, M.N. *et al.* Large, non-saturating magnetoresistance in WTe₂. *Nature* **514**, 205 (2014).
- [26] Chang, T.-R. *et al.* Arc-tunable Weyl fermion metallic state in Mo_xW_{1-x}Te₂. Preprint at <http://arxiv.org/abs/1508.06723> (2015).
- [27] Qi, Y. *et al.* Superconductivity in Weyl semimetal candidate MoTe₂. Preprint at <http://arxiv.org/abs/1508.03502> (2015).
- [28] Pletikosić, I. Ali, Mazhar N. Fedorov, A. V. Cava, R. J. Valla, T. Electronic structure basis for the extraordinary magntoresistance in WTe₂. *Phys. Rev. Lett.* **113**, 216601 (2014).
- [29] Wu, Y. *et al.* Temperature-induced Lifshitz transition in WTe₂. *Phys. Rev. Lett.* **115**, 166602 (2015).

- [30] Jiang, J. *et al.* Signature of strong spin-orbital coupling in the large nonsaturating magnetoresistance material WTe₂. *Phys. Rev. Lett.* **115**, 166601 (2015).
- [31] Beloposki, I. *et al.* Unoccupied electronic structure and signatures of topological Fermi arcs in the Weyl semimetal candidate Mo_xW_{1-x}Te₂. Preprint at <http://arxiv.org/abs/1512.09099> (2016).
- [32] Clarke, R., Marseglia, E. & Hughes, H.P. A low-temperature structural phase transition in β -MoTe₂. *Phil. Mag. B* **38**, 121 (1978).
- [33] Manolikas, C., Van Landuyt, J. & Amelinckx, S. Electron microscopy and electron diffraction study of the domain structures, the dislocation fine structure, and the phase transformations in β -MoTe₂. *Phys. Stat. Sol.* **53**, 327 (1979).
- [34] Keum, D.H. *et al.* Bandgap opening in few-layered monoclinic MoTe₂. *Nature Phys.* **11**, 482 (2015).
- [35] Wang, J. *et al.* Power-law decay of standing waves on the surface of topological insulators. *Phys. Rev. B* **84**, 235447 (2011).
- [36] T. Zhang, P. Cheng, X. Chen, J.-F. Jia, X. Ma, K. He, L. Wang, H. Zhang, X. Dai, Z. Fang, X. Xie, and Q.-K. Xue. Experimental Demonstration of Topological Surface States Protected by Time-Reversal Symmetry. *Phys. Rev. Lett.* **103**, 266803 (2009).
- [37] L. Huang *et al.* Spectroscopic evidence for type II Weyl semimetal state in MoTe₂. arXiv:1603.06482.
- [38] Kresse, G. and Furthmüller, J. Efficient iterative schemes for ab initio total-energy calculations using a plane-wave basis set. *Phys. Rev. B* **54**, 11169 (1996).

Acknowledgements This work is supported by the National Natural Science Foundation of China (grant No. 11274191, 11334006), Ministry of Science and Technology of China (No. 2015CB921001 and 2012CB932301) and Tsinghua University Initiative Scientific Research Program (No. 2012Z02285). The Advanced Light Source is supported by the Director, Office of Science, Office of Basic Energy Sciences, of the US Department of Energy under Contract No. DE-AC02-05CH11231.

Author Contributions S.Z., X.C. and Y.W. conceived the research project. K.D. and K.Z. grew and characterized the samples under supervision of Y.W.. K.D., G.W, K.Z., S.D., E.W., M.Y., and H.Y.Z. performed the ARPES measurements and analyzed the ARPES data. J.D. and A. F. provided support for the ARPES experiments. P.D. and Z.X. performed

the STM measurements. H.J.Z. performed the first principle calculations. K.D., H.Y., Y.W., X.C. and S.Z. wrote the manuscript, and all authors commented on the manuscript.

Competing financial interests The authors declare no competing financial interests.

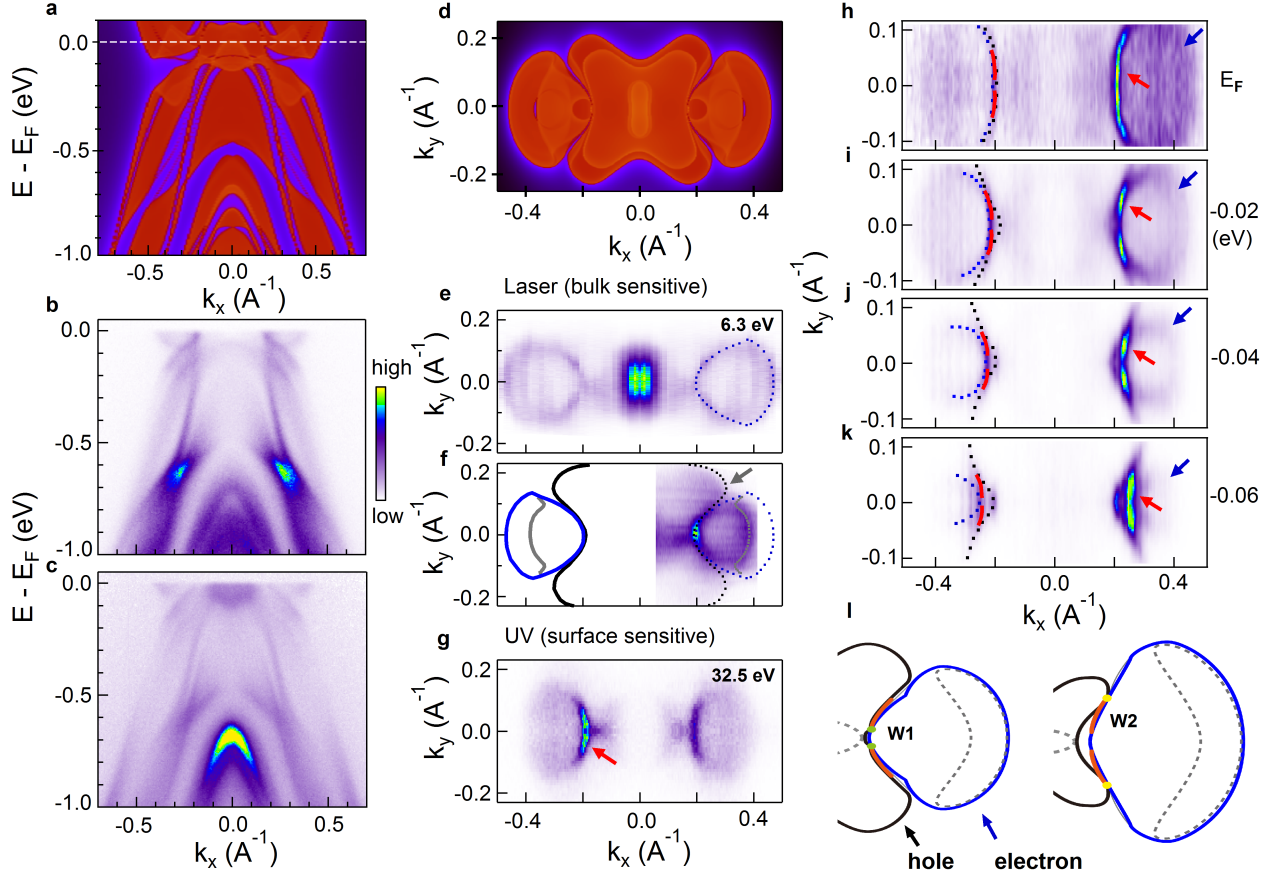


FIG. 3: **Signatures of Fermi arcs in the T_d phase of MoTe_2 .** (a) Calculated surface energy dispersion along the $\bar{X}-\bar{\Gamma}-\bar{X}$ direction. The dots label the positions for the Weyl points W2. (b,c) Measured dispersions along the $\bar{X}-\bar{\Gamma}-\bar{X}$ direction with horizontal (p) and vertical (s) polarizations at photon energy of 32.5 eV. (d) Calculated Fermi surfaces projected on the (001) plane. (e,f) Fermi surface maps measured using 6.3 eV laser source with light polarization parallel to the b-axis and a-axis respectively. (g) Fermi surface map measured with p-polarization at 32.5 eV photon energy. (h-k) High resolution intensity maps measured at energies from E_F to -0.06 eV with p-polarization. Maps in panels (g-k) were obtained by symmetrizing data taken at positive k_y values. The blue arrows point to the electron pockets which decrease in size from E_F to -0.06 eV, and the red arrow point to the arc-like feature. (l) Schematic cartoon to show the Weyl points W1 (green dots), W2 (yellow dots) and the Fermi arcs (red curve).

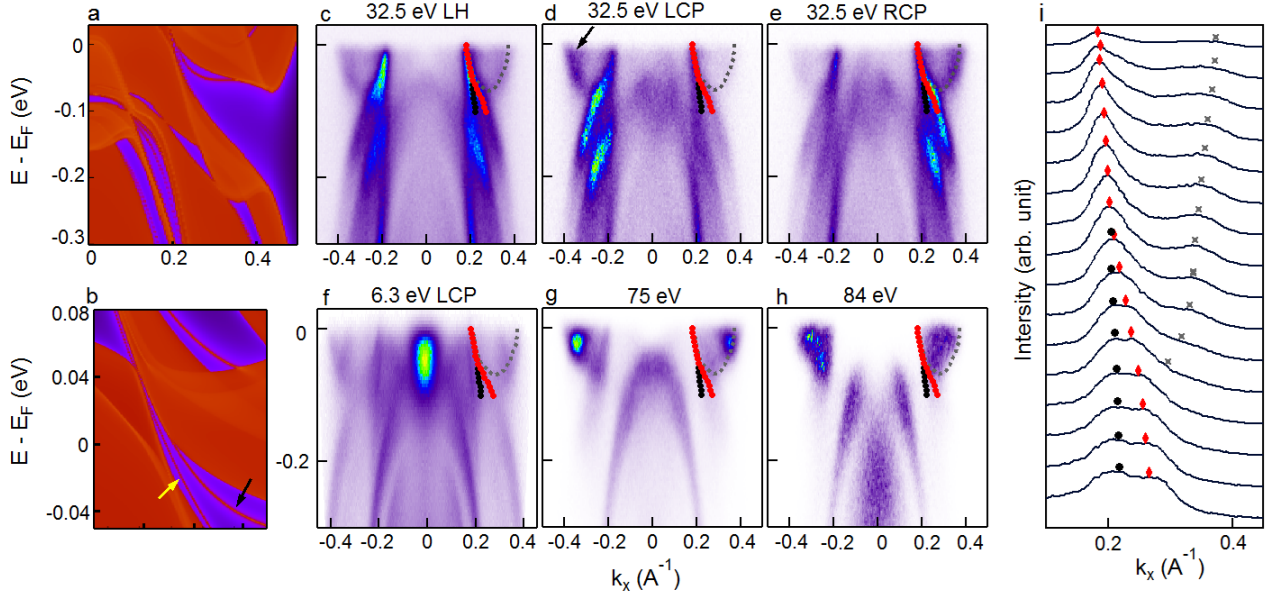


FIG. 4: **Dispersion of the surface states.** (a) Calculated dispersions parallel to the $\bar{X}-\bar{\Gamma}-\bar{X}$ direction at $k_y = 0.06 \text{ \AA}^{-1}$. (b) Zoom-in of the calculated dispersions to show the topological surface states (yellow arrow) and trivial surface states (black arrow). (c-h) Measured dispersion along the $\bar{X}-\bar{\Gamma}-\bar{X}$ direction with different light polarizations and photon energies. (i) MDCs for data taken in panel (c) from E_F to -0.1 eV. The peak dispersions for the linear and shoulder-like dispersions are marked by symbols. The extracted dispersions are overplotted in all panels to show that the shoulder-like dispersion (red curve) does not depend on photon energy (k_z effectively).

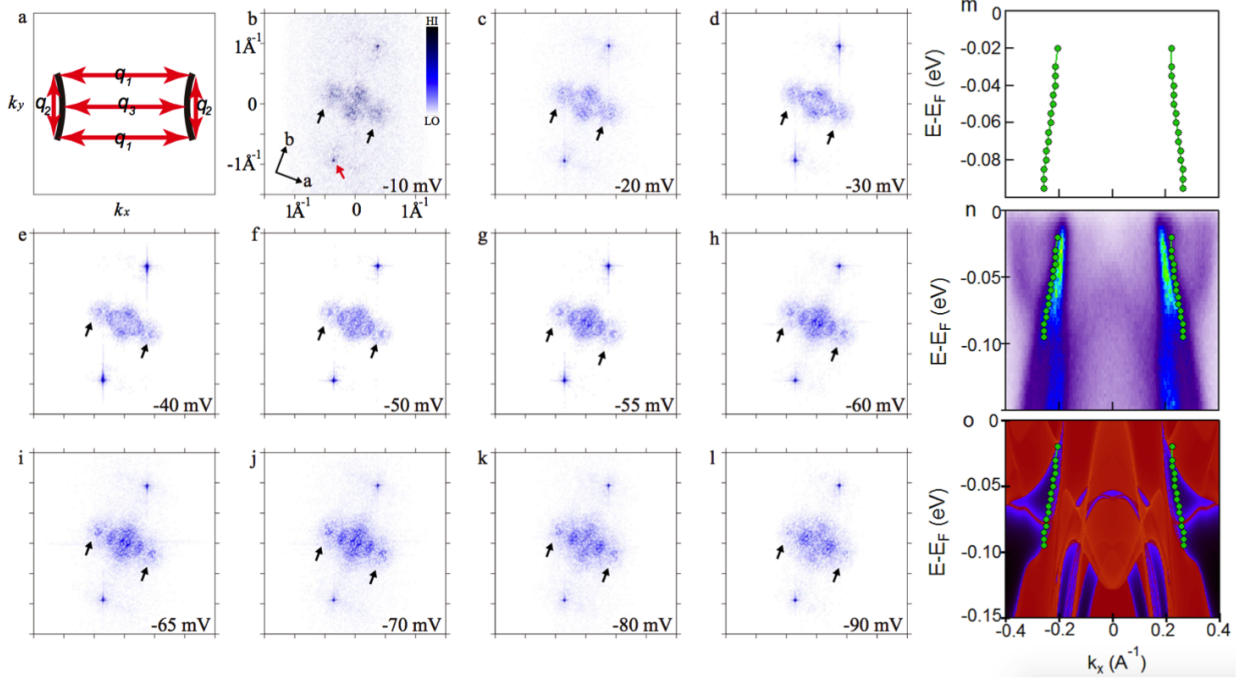


FIG. 5: **Quasi-particle interference pattern.** (a) The dominant scattering vectors owing to a pair of Fermi arcs. (b-l) The FFT power spectra of the dI/dV maps of a region shown in supplementary information. The current was set at 0.1 nA. Each map has 256×256 pixels. The temperature is 4.2 K. The features for q_1 are indicated by black arrows. The origin of the additional features in QPI needs further investigation. The red arrow points to a Bragg peak. (m-o) Dispersions of the Fermi arc extracted from QPI and comparison with ARPES measurements and calculated dispersions.